Quantitative Susceptibility Mapping: Basic Methods and Clinical Applications

Taisuke Harada, MD, PhD
Kohsuke Kudo, MD, PhD
Noriyuki Fujima, MD, PhD
Masato Yoshikawa, MD, PhD
Yohei Ikebe, MD, PhD
Ryota Sato, PhD
Toru Shirai, MS
Yoshitaka Bito, PhD
Ikuko Uwano, PhD
Mari Miyata, MD

From the Department of Diagnostic Imaging, Hokkaido University Graduate School of Medicine, N15 W7, Kita-ku, Sapporo, Japan (T.H., K.K., M.Y.); Center for Cause of Death Investigation (T.H.) and Global Center for Biomedical Science and Engineering (K.K.), Faculty of Medicine, Hokkaido University, Sapporo, Japan; Department of Diagnostic and Interventional Radiology, Hokkaido University Hospital, Sapporo, Japan (T.H., K.K., N.F., M.Y., Y.I.); Innovative Technology Laboratory, Fujifilm Healthcare Corporation, Tokyo, Japan (R.S., T.S.); Fujifilm Healthcare Corporation, Chiba, Japan (Y.B.); Division of Ultrahigh Field MRI, Institute for Biomedical Sciences, Iwate Medical University, Yahaba, Japan (I.U.); and Department of Functional Brain Imaging, Institute for Quantum Medical Science, Quantum Life and Medical Science Directorate, National Institutes for Quantum Science and Technology, Chiba, Japan (M.M.). Presented as an education exhibit at the 2020 RSNA Annual Meeting. Received March 8, 2021; revision requested September 3 and received September 19; accepted October 20. For this journal-based SA-CME activity, the authors K.K., R.S., T.S., and Y.B. have provided disclosures (see end of article); all other authors, the editor, and the reviewers have disclosed no relevant relationships. **Address correspondence to** K.K. (e-mail: *kkudo@med.hokudai.ac.jp*).

Quantitative susceptibility mapping (QSM), one of the advanced MRI techniques for evaluating magnetic susceptibility, offers precise quantitative measurements of spatial distributions of magnetic susceptibility. Magnetic susceptibility describes the magnetizability of a material to an applied magnetic field and is a substance-specific value. Recently, QSM has been widely used to estimate various levels of substances in the brain, including iron, hemosiderin, and deoxyhemoglobin (paramagnetism), as well as calcification (diamagnetism). By visualizing iron distribution in the brain, it is possible to identify anatomic structures that are not evident on conventional images and to evaluate various neurodegenerative diseases. It has been challenging to apply QSM in areas outside the brain because of motion artifacts from respiration and heartbeats, as well as the presence of fat, which has a different frequency to the proton. In this review, the authors provide a brief overview of the theoretical background and analyze methods of converting MRI phase images to QSM. Moreover, we provide an overview of the current clinical applications of QSM.

Online supplemental material is available for this article.

©RSNA, 2022 • radiographics.rsna.org

SA-CME LEARNING OBJECTIVES

After completing this journal-based SA-CME activity, participants will be able to:

■ Describe magnetic susceptibility and reconstruction of QSM.

■ Differentiate between calcification and hemorrhage at QSM.

■ Recognize the pathophysiologic basis of neurodegenerative disorders and identify the sites of iron deposition in each disorder.

See rsna.org/learning-center-rg.

Introduction

Quantitative susceptibility mapping (QSM) is a relatively new MRI technique developed in the past 10 years for quantifying the amount and spatial distribution of magnetic susceptibility (1). Conventional gradient-echo (GRE) T2*-weighted imaging has been widely used in clinical settings to depict abnormal magnetic susceptibility, such as that observed in long-term hemorrhage and calcification (2). However, because conventional T2*-weighted imaging is two-dimensional, the resolution in the section direction is poor, and the detection sensitivity is low because of problems related to the section gap and section position shift. Susceptibility-weighted imaging (SWI) was developed on the basis of T2* contrast-enhanced imaging and has high spatial resolution due to three-dimensional acquisition and a high detection rate of hemorrhage due to use of magnitude and phase information. However,

TEACHING POINTS

- Magnetic susceptibility (χ) is a substance-specific material property that describes the response of the substance of an object to being placed within a magnetic field.

- Therefore, calcification and hemorrhage are easy to distinguish with QSM because the magnetic susceptibility is indicated as low and high contrast, respectively.

- In diseases that manifest with abnormal iron deposition such as NBIA, it is necessary to consider whether the iron deposition is age appropriate, as a similar level of iron deposition in the basal ganglia may be abnormal in children but within normal limits in elderly adults.

- Therefore, serial QSM provides information regarding the current state of inflammation within multiple sclerosis lesions. Lesions with no increase in magnetic susceptibility are acute or older than 5 years, while those with increased magnetic susceptibility indicate the possibility of several weeks to years after onset.

- The theory behind generating OEF maps from QSM is based on the idea that the susceptibility of veins is higher than that of brain parenchyma because of the elevated deoxyhemoglobin concentration.

neither is quantitative, and both often contain blooming artifacts. R2* (transverse relaxation rate) is also used to evaluate magnetic susceptibility quantitatively. However, this parameter is affected by an inhomogeneous magnetic field and geometry orientation relative to the static field, resulting in measurement errors (3). Additionally, both hemorrhage and calcification produce low signal intensity and cannot be distinguished.

In contrast, QSM is a quantitative image that can help differentiate between hemorrhage and calcification by depicting the magnetic susceptibility and can eliminate the negative effects observed at SWI in the process of reconstruction. Moreover, QSM is now being applied in clinical practice (1). The Table and Figure 1 summarize the characteristics of the imaging sequences used to evaluate the magnetic susceptibility and the types of images required for reconstruction. In this article, we review the basics of the biophysics and analytical methods of QSM and provide an overview of its clinical applications.

Basic Methods

Magnetic Susceptibility to Magnet Field

Magnetic susceptibility (χ) is a substance-specific material property that describes the response of the substance of an object to being placed within a magnetic field. Each magnetization generates an additional magnetic field called a magnetic dipole field (Fig 2). Around a paramagnetic body, the magnetic field in the same direction as that of the static magnetic field becomes stronger. Conversely, the magnetic field in the transverse

direction becomes weaker (4). As a result, the local magnetic field increases for a paramagnetic material in a static magnetic field. In contrast, it decreases for diamagnetic materials (Fig E1). QSM can demonstrate the magnetic susceptibility of paramagnetic and diamagnetic materials through positive and negative values as high- and low-contrast images.

How to Reconstruct QSM

The following image processing steps are required to extract the local susceptibility from magnitude and phase images. These steps include image acquisition, region extraction, phase unwrapping, background field removal, and magnetic dipole inversion (Fig 3).

1. Image acquisition. The phase and magnitude images acquired by using the three-dimensional GRE method are required as the input data. For QSM reconstruction, multiecho acquisition is recommended because a single-echo acquisition cannot accurately measure the magnetic field changes in all tissues (4,5). Regarding the imaging parameters, the last echo time (TE) should be the same or an approximately similar value as the T2* value of the specific tissue to maximize the signal-to-noise ratio, and it is recommended that the last TE should be 30–40 msec and the echo space be within 5 msec for brain imaging (6,7). The section thickness should be less than 2 mm, and thin sections are recommended for evaluation of small magnetic substances to exclude partial volume effect.

2. Region extraction. The region where the QSM is to be calculated is extracted to exclude the effects of great phase changes such as those of air, bone, and fat (1).

3. Phase unwrapping. Since the phase image contains multiple phase wrappings, phase unwrapping by using the region-growing algorithm or Laplacian-based method is applied (1).

4. Background field removal. Because the whole magnetic field has inhomogeneities affected by various magnetic sources outside the target, background field removal is performed to obtain a local magnetic field by using the regularization-enabled sophisticated harmonic artifact reduction (RESHARP) method or the projection onto dipole fields method.

5. Magnetic dipole inversion. Local susceptibility is determined by deconvolution with the magnetic field of the dipole kernel in the k-space (Fig E2). This step is called dipole inversion (1,5,8).

Clinical Applications

In clinical practice, T2*-weighted imaging and SWI have been used to evaluate many disorders that affect magnetic susceptibilities, such as

Imaging Sequences in Evaluation of Magnetic Susceptibility

Imaging Sequence	Acquisition	Number of Echoes	Quantitative Value	Discrimination between Diamagnetic and Para-magnetic Substances	Postprocessing	Blooming Artifact
T2*WI	2D	Single	No	No	No	Yes
R2*	2D or 3D	Multiple	Yes	No	Yes (simple) curve fitting	Yes
SWI	3D	Single	No	No	Yes (intermediate) phase unwrapping and phase mask	Yes
QSM	3D	Single or multiple	Yes	Yes	Yes (complex) phase unwrapping, background field removal, and dipole inversion	No

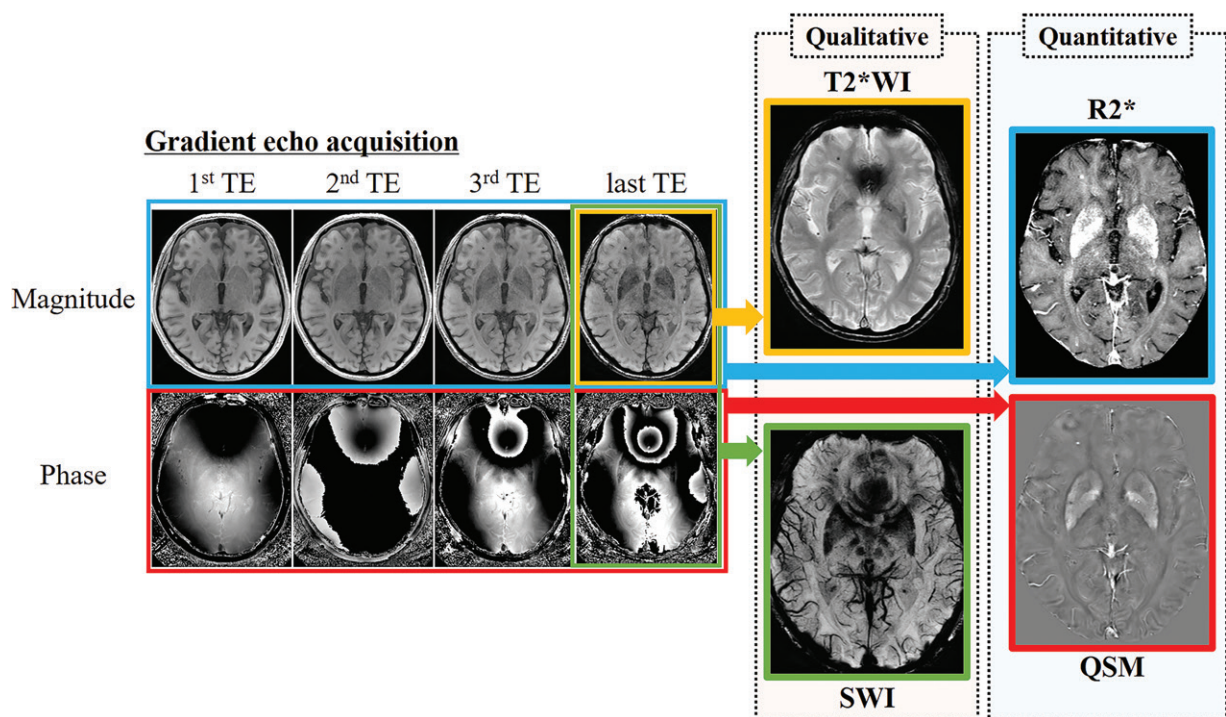Note.—3D = three-dimensional, T2*WI = T2*-weighted imaging, 2D = two-dimensional.

Figure 1.   Diagram of the relationship between the image and source data for evaluation of magnetic susceptibility. SWI, R2*, and QSM are reconstructed from the data obtained from a gradient multiecho acquisition. SWI (green box) is based on a set of magnitude and phase images with a long echo time (TE), and the magnitude image is multiplied by the phase image several times. R2* (blue box) is obtained as the reciprocal of the T2* value (1/T2*), and the T2* value can be calculated from multiple magnitude images. QSM (red box) uses multiple phase images to perform multiple reconstruction steps. T2*-weighted imaging *(T2*WI)* (yellow box) does not require any reconstruction process.

traumatic intracranial hemorrhage and microhemorrhage with hemosiderin, neurodegenerative disorders and demyelinating disease with iron deposition, stroke with thrombus, and vascular malformation with veins (9). SWI is a qualitative method and can depict only the presence of abnormal magnetic susceptibility. Therefore, it cannot help differentiate positive and negative magnetic susceptibility values. In contrast to SWI, QSM can express magnetic susceptibility values for deoxyhemoglobin, iron (ferritin), and hemosiderin as para-

magnetic substances and myelin, oxyhemoglobin, and calcification as diamagnetic substances. In the brain, contrasts of QSM consist of high-contrast paramagnetic substances such as the cortex and deep gray matter containing ferritin; hemorrhage and microbleeds containing deoxyhemoglobin, methemoglobin, and hemosiderin; veins containing high amounts of deoxyhemoglobin; low-contrast diamagnetic substances such as white matter–containing myelin; and choroid plexus, containing calcification (Fig 4) (10). Many morphologic
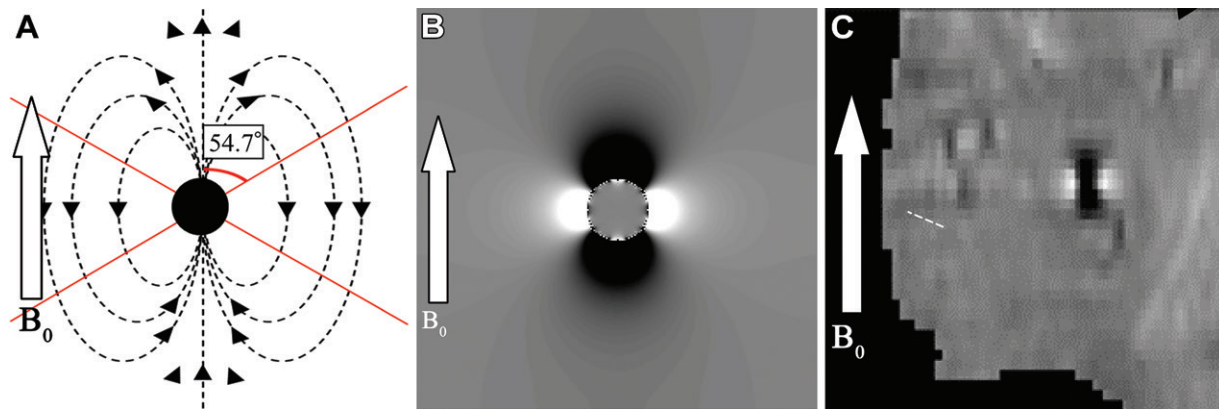
Figure 2. Magnetic dipole field. **(A)** Magnetic dipole field in a situation of paramagnetic material in a static magnetic field. **(B)** Phase map of the same simulation with a paramagnetic object placed in a static magnetic field viewed from a parallel direction to B_0. **(C)** Coronal unwrapped phase map around microbleeds in vivo. A magnetic field (dashed line) can be observed forming around the paramagnetic material. There are also lobes of positive and negative field strength, which are defined as areas of relative high and low contrast, respectively, in the simulation **(B)** and in vivo **(C)**. B_0 is the direction of the static magnetic field.
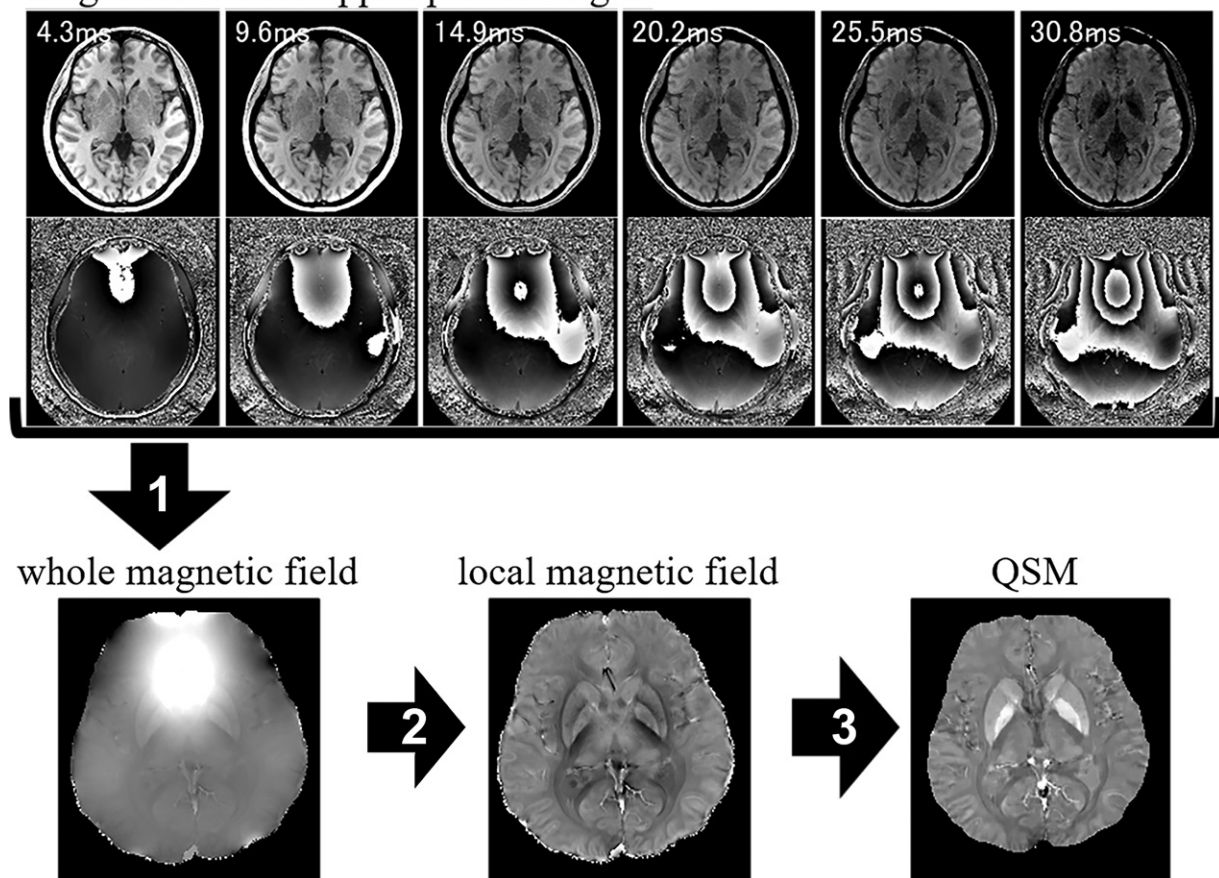

Figure 3. Process steps for converting GRE images into magnetic susceptibility. The QSM pipeline from multiple three-dimensional, gradient-echo, multiple-TE images (magnitude images in upper row and phase images in lower row) to QSM consists of the following steps: phase unwrapping *(1)*, background field removal *(2)*, and dipole inversion *(3)*. *ms* = milliseconds.

structures with different susceptibility values can be clearly observed with QSM because of the high spatial resolution and differences in magnetic susceptibility. Table E1 summarizes a list of diseases, contrasts, abnormal sites, and corresponding substances that can be depicted with QSM.

Hemorrhage and Calcifications

With QSM, hemorrhage and calcification are visualized as areas of high and low contrast, respectively. Hemorrhage and calcification are frequently seen in many intracranial diseases. For example, hemorrhages may be observed
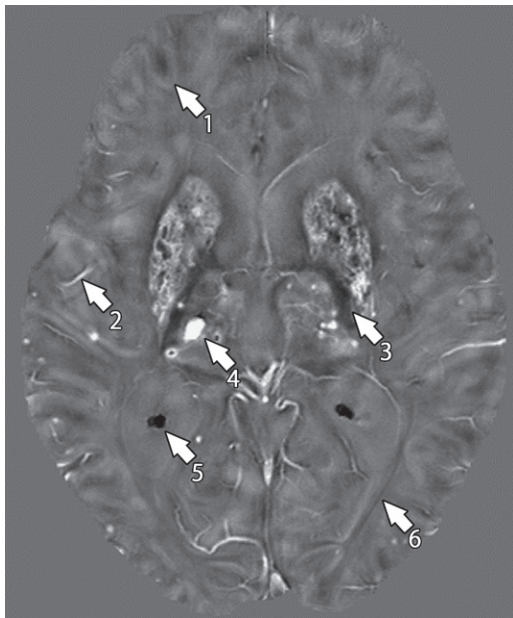
Figure 4. Contrast of QSM in the brain. The QSM image clearly reveals the corticomedullary junction *(1)*, cortical vein (deoxyhemoglobin) *(2)*, internal capsule (myelin) *(3)*, microbleeds in the thalamus (hemosiderin) *(4)*, calcification of the choroid plexus *(5)*, and optic radiation (myelin) *(6)*. The basal ganglia show higher contrast than the surrounding myelin because of iron deposition and microhemorrhage, whereas the inside contains areas of low contrast that are suggestive of calcification.

in hemorrhagic stroke, traumatic brain injury, vascular malformation, or malignant glioma, whereas calcifications are often observed in tuberous sclerosis, tuberculosis, Sturge-Weber syndrome, neurocysticercosis, oligodendroglioma, meningioma, or craniopharyngioma (11). Thus, detection of hemorrhage or calcification can be key for the differential diagnosis.

Conventional MRI, including T2*-weighted imaging and SWI, cannot help distinguish between hemorrhage and calcification because both show nonspecific low signal intensity. By using phase images, microbleeds and microcalcifications can be differentiated because of opposite phase shifts, since small lesions often show simple and clear phase changes. However, in large irregularly shaped lesions, the phase shape is complicated, and imaging parameters—such as section thickness—affect the delineation and make it difficult to differentiate between them (9). Coarse calcification can be assessed with the T1 surface effect, but small lesions are difficult to evaluate.

CT can help differentiate between calcification and hemorrhage with differences in attenuation. However, these differences can be difficult to identify in faint or small lesions and require ionizing radiation. An analysis of the magnetic susceptibility of hematomas indicated that magnetic susceptibilities of deoxyhemoglobin (acute hematoma), intracellular methemoglobin (early subacute), and extracellular methemoglobin (late subacute) provide higher values and are visualized as areas that have higher contrast than the surrounding tissues or myelin (12). In contrast, calcification is a strong diamagnetic substance and is visualized as low contrast with QSM.

Therefore, calcification and hemorrhage are easy to distinguish with QSM because the magnetic susceptibility is indicated as low and high contrast, respectively. SWI is considered to be more sensitive than T2*-weighted imaging in evaluation of microbleeds. Further, it has been reported that hemorrhage depiction is comparable between SWI and QSM (13).

The ability to identify calcified and hemorrhagic tumor areas may be valuable for differentiating and grading brain tumors (14). For instance, oligodendroglioma often shows coarse calcification within the tumor. Although this calcification may be easily identified at CT, very small or punctate calcifications are difficult to identify at CT. Even with MRI, it is often difficult to distinguish calcification from small hemorrhages because of its faint low signal intensity (Fig 5).

High-grade gliomas such as glioblastoma and metastatic brain tumors derived from melanoma, renal, and lung carcinomas are often associated with hemorrhage, but chemotherapy drugs such as bevacizumab (a vascular endothelial growth factor inhibitor) can also cause calcification within the tumor as a therapeutic effect. QSM can help distinguish between intratumoral hemorrhage and treatment-responsive intratumoral calcification (15). As shown in Figure 6, meningioma demonstrates the coexistence of calcification and hemorrhage within the tumor at QSM, which is an imaging finding that cannot be revealed with conventional imaging modalities such as T2*-weighted imaging, SWI, and CT.

Physiologic Iron Deposition
At QSM, the basal ganglia, substantia nigra, and red nucleus are more clearly depicted as high contrasts in elderly people than in young individuals because of the progressive deposition of paramagnetic iron with aging. Iron in the brain is regulated by a number of proteins to ensure homeostasis. The systemic circulation is physically separated from the brain tissue by two cellular barriers, the blood-brain barrier and the blood–cerebrospinal fluid barrier. Iron transports across these barriers by microvascular endothelial cells in the brain and holo-transferrin.

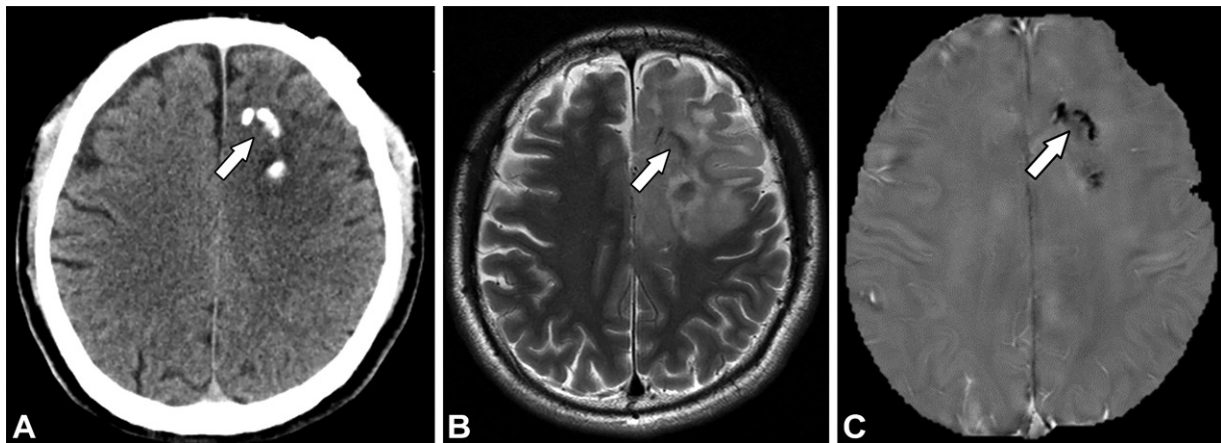Neurons and astrocytes acquire transferrin-bound or non–transferrin-bound iron, and

Figure 5. Oligodendroglioma in a 28-year-old man. **(A)** Axial CT image demonstrates a club-shaped calcification (arrow) in the left frontal lobe, which is a typical imaging finding in oligodendroglioma. **(B)** Axial T2*-weighted MR image shows faint low signal intensity (arrow) within the high signal intensity area. **(C)** QSM image demonstrates an area of definite low contrast (arrow), indicating calcification as a diamagnetic substance.
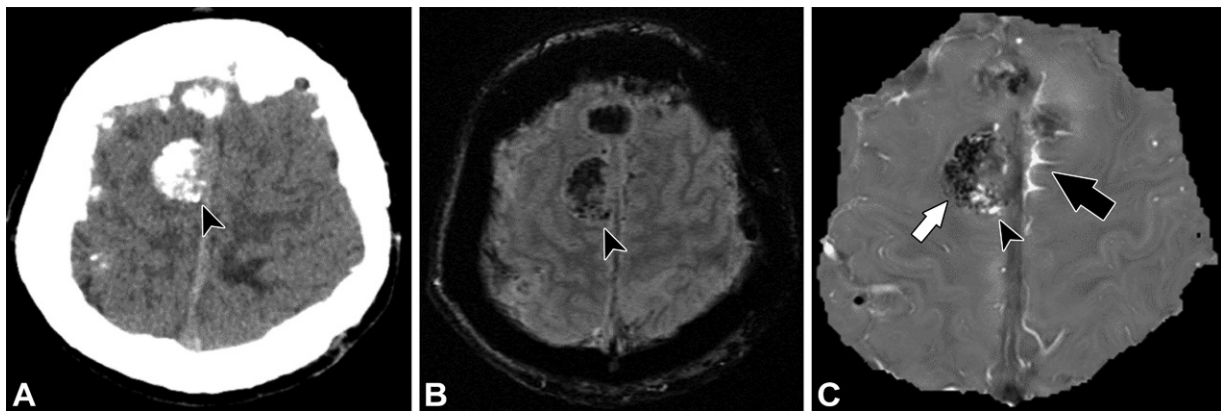

Figure 6. Meningioma of neurofibromatosis type 2 in a 34-year-old woman. **(A)** Axial CT image shows a high-attenuation nodule close to the falx (arrowhead). **(B)** Axial T2*-weighted MR image shows an area of signal hypointensity (arrowhead), which is suggestive of calcification or hemorrhage. **(C)** Axial QSM image demonstrates mixed signal intensity with areas of low and high contrast, indicating the coexistence of calcification (white arrow) and hemorrhage (arrowhead). Additionally, the QSM image shows hemosiderin deposition in the medial left frontal lobe (black arrow).

microglia phagocytose cells to recycle iron, with excess iron being stored with ferritin. Ferritin is the principal storage protein used to sequester iron in neurons and glia, as well as many other cell types. Excess iron is either sequestrated by ferritin or exported from the cells by ferroportin. Intracellular iron levels are regulated by binding to the iron-responsive elements of mRNA of iron regulatory proteins. These cells and proteins form iron homeostasis through complex cellular molecular mechanisms. Iron dyshomeostasis has become a molecular signature associated with aging and is accompanied by a progressive decline in cognitive processes (16).

Throughout life, iron deposition increases progressively in the gray and white matter of the brain (Fig 7) (17). Aquino et al (18) have reported that magnetic susceptibility of the basal ganglia is low in people younger than 10 years of age, and

these findings are consistent with reports that iron deposition is rarely observed in newborns. Li et al (19) demonstrated that the age-related magnetic susceptibility continues to increase over time and manifests as high contrast at QSM in the putamen, as well as in the globus pallidus, caudate nucleus, red nucleus, and substantia nigra until around the age of 30 years, which is when the susceptibility level reaches a plateau. In the subcortical white matter in the motor and sensory cortexes, the magnetic susceptibility continues to increase with age, as observed in the putamen. Magnetic susceptibility of the white matter shows a consistent biphasic temporal pattern, with an initial decrease followed by an increase in susceptibility. This characteristic trend is consistent with that of myelin maturation and turnover in the course of normal brain development until the age of 20 years, and thereafter increases with age (19).
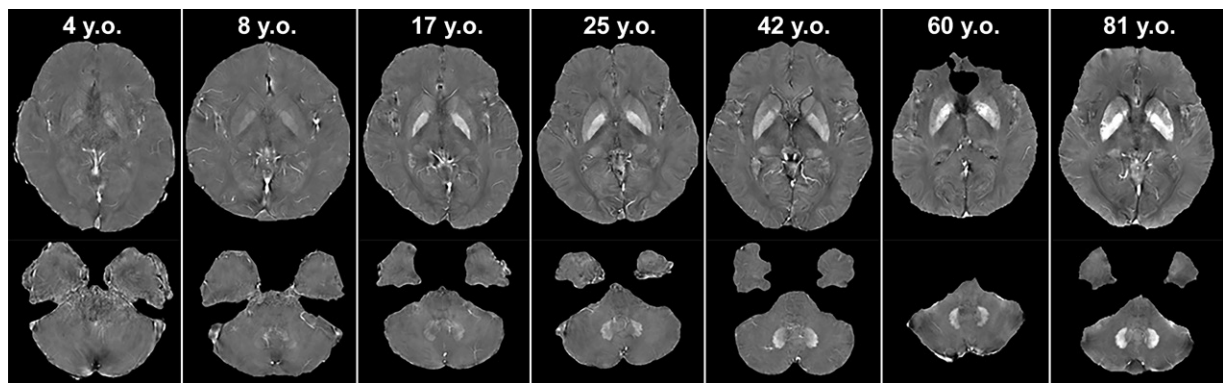
Figure 7. Age-related iron deposition in healthy individuals. Axial QSM images depict how the magnetic susceptibility of the basal ganglia and cerebellar dentate nuclei increases with age, with mild iron deposition at ages younger than 10 years old *(y.o.)* and well-defined iron deposition around the age of 20 years.

Figure 8. Brain anatomy in a healthy volunteer with high-resolution QSM at 3-T MRI (spatial resolution = 0.22 × 0.22 × 0.50 mm). **(A–E)** Axial QSM images clearly show the caudate nucleus *(1)*, putamen *(2)*, globus pallidus *(3)*, pulvinar *(4)*, optic radiation *(5)*, stria of Gennari *(6)*, anterior nuclei of the thalamus *(7)*, mediodorsal nucleus of the thalamus *(8)*, substantia nigra *(9)*, red nucleus *(10)*, and transverse pontine fibers *(11)*. **(F)** Coronal QSM image depicts the subthalamic nucleus *(12)* above the substantia nigra *(9)*.

Anatomic Imaging of the Brain

Some structures in the brain are difficult to visualize with conventional imaging but can be easily observed with QSM. For example, basal ganglia such as the caudate nucleus, putamen, and globus pallidus are prominent sites of iron deposition, and it is possible to separate the internal, medial, and external globus pallidus (5). The thalamus also contains iron, and the anterior nucleus, mediodorsal nucleus, and pulvinar of the thalamus contain enough iron to be visualized as high contrast (Fig 8). The subthalamic nucleus is located directly above the substantia nigra and is the target of deep stimulation therapy for Parkinson disease (Fig 8). QSM provides high spatial

resolution and high contrast-to-noise ratio, can more clearly depict the subthalamic nucleus than SWI and T2*-weighted imaging, and has been applied clinically as a surgical aid (20).

The primary motor cortex, primary sensory cortex, auditory cortex, and visual cortex have particularly high myelin densities but show slightly higher contrast at QSM, probably because of co-localization of iron and myelin and increased magnetic susceptibility caused by iron (21). Figure 8 shows a clearly delineated stria of Gennari in the visual cortex, which is a band of myelinated axons that runs parallel to the surface of the cerebral cortex. In contrast, the corticospinal tract, posterior limb of the internal capsule,

and optic radiation appear with low contrast at QSM, indicating a high diamagnetic myelin density. In the posterior fossa, iron deposits in the red nucleus, substantia nigra, and dentate nucleus of the cerebellum are well delineated, and transverse fibers of the pontine are seen as linear low contrasts at QSM.

The contrast between cortex and white matter is mainly determined by myelin. However, iron deposition may also affect its contrast because iron deposition in subcortical U fibers in the temporal lobe is estimated to be two- to eightfold higher than that in cortical gray matter (17,22).

The maximum intensity projection (MIP) of QSM can be used to produce high-spatial-resolution venography (Fig 9). QSM venography is capable of visualizing not only large veins such as the cortical and internal cerebral veins, but also the medullary vein and small veins distributed in the deep gray matter such as the thalamostriate and terminal stria veins, which are difficult to visualize with conventional sequences such as contrast-enhanced GRE MR venography.

Neurodegeneration with Brain Iron Accumulation

Iron dyshomeostasis, a common theme in neurodegenerative diseases, is associated with neuroinflammation, abnormal protein aggregation, neurodegeneration, and neurobehavioral deficits.

Neurodegeneration with brain iron accumulation (NBIA) describes a rare, inherited, neurologic movement disorder characterized by abnormal iron accumulation in the brain, especially the globus pallidus, demonstrating bright contrast at QSM. Clinical major symptoms comprise early-onset dystonia and pyramidal and extrapyramidal signs, with ataxia, cognitive decline, behavioral abnormalities, and retinal and axonal neuropathy (23). NBIA is first suspected when increased basal ganglia iron level is observed at MRI (as shown in Fig 10), and QSM may be able to easily depict age-inappropriate iron deposition in the globus pallidus as high contrast (24). In diseases that manifest with abnormal iron deposition such as NBIA, it is necessary to consider whether the iron deposition is age appropriate, as a similar level of iron deposition in the basal ganglia may be abnormal in children but within normal limits in elderly adults.

Idiopathic Basal Ganglia Calcification (Fahr Disease)

Basal ganglia calcifications at CT are incidental findings in up to 20% of asymptomatic adult patients but are rare in healthy children. Therefore, idiopathic basal ganglia calcification or Fahr disease is suspected when symmetrical calcification
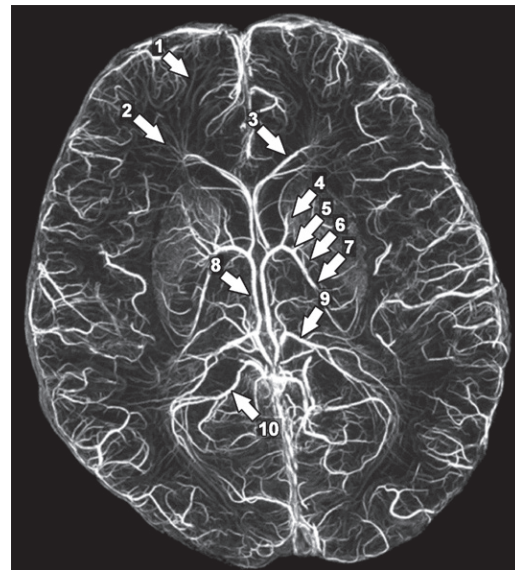

Figure 9. High-resolution venography with MIP of venous-extracted high-resolution QSM at 3-T MRI (spatial resolution = 0.22 × 0.22 × 0.50 mm). Axial QSM venogram clearly reveals the following small veins: superficial medullary *(1)*, deep medullary *(2)*, septal *(3)*, anterior caudate *(4)*, thalamostriate *(5)*, posterior caudate *(6)*, stria terminalis *(7)*, internal cerebral *(8)*, direct lateral *(9)*, and basal *(10)*.

is observed from childhood, not only in the basal ganglia but also in the subcortical and dentate nuclei (25). All areas corresponding to calcification at CT show low signal intensity at T2*-weighted imaging, and we expected all of these areas to show low contrast at QSM. However, in our experience, the basal ganglia and dentate nuclei show high contrast at QSM (Fig 11).

The reason for this may be because of ectopic mineralization, which includes iron, lead, copper, and manganese rather than merely calcium deposition (26,27). The increase in magnetic susceptibility may occur because of inorganic paramagnetic materials, which overwhelm the decrease in magnetic susceptibility because of calcification and may be accompanied by iron deposition due to neurodegeneration in the basal ganglia. Therefore, the imaging findings described as calcification at CT may be interpreted as mineralization, including rich inorganic paramagnetic materials, and QSM may provide new insight into the pathogenesis of conditions that were previously thought to be caused by calcification by helping distinguish them from mineralization.

In addition, increased magnetic susceptibility of the basal ganglia, thalamus, and cerebellar dentate nucleus has been observed in systemic lupus erythematosus (SLE), Wilson disease, liver cirrhosis, and depression; decreased magnetic susceptibility of the whole brain, including the basal ganglia, thalamus, and white matter, has been suggested in pediatric patients with autism (28–32).
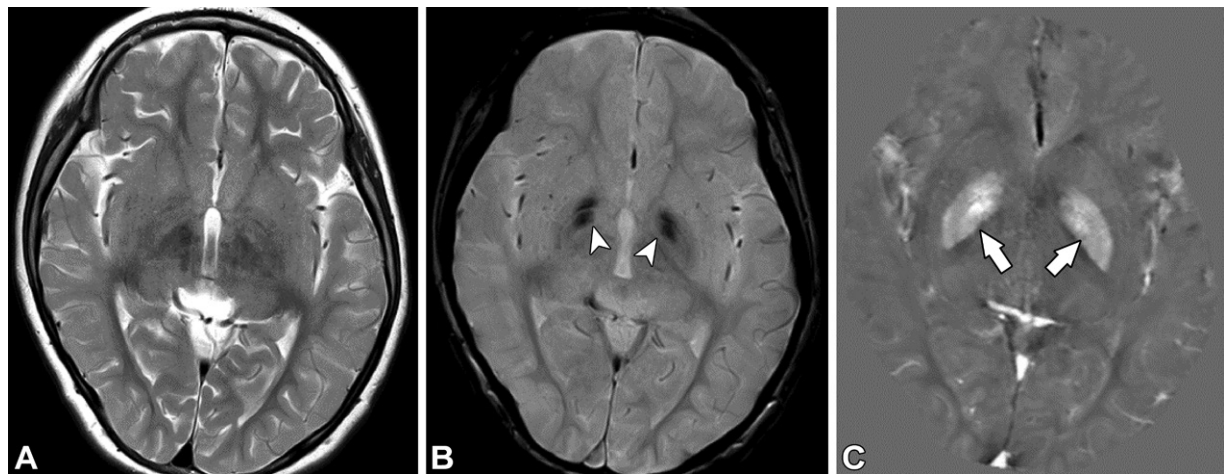
Figure 10.   NBIA 5 in an 8-year-old boy. **(A)** Axial T2*-weighted MR image shows no abnormality around the basal ganglia. **(B)** Axial T2*-weighted MR image shows focal hypointensity in the anterior part of the globus pallidus (arrowheads). **(C)** QSM image clearly demonstrates high contrast in the entire bilateral globus pallidus (arrows), suggesting abnormal iron deposition compared with that in healthy patients of the same age (see Fig 6).
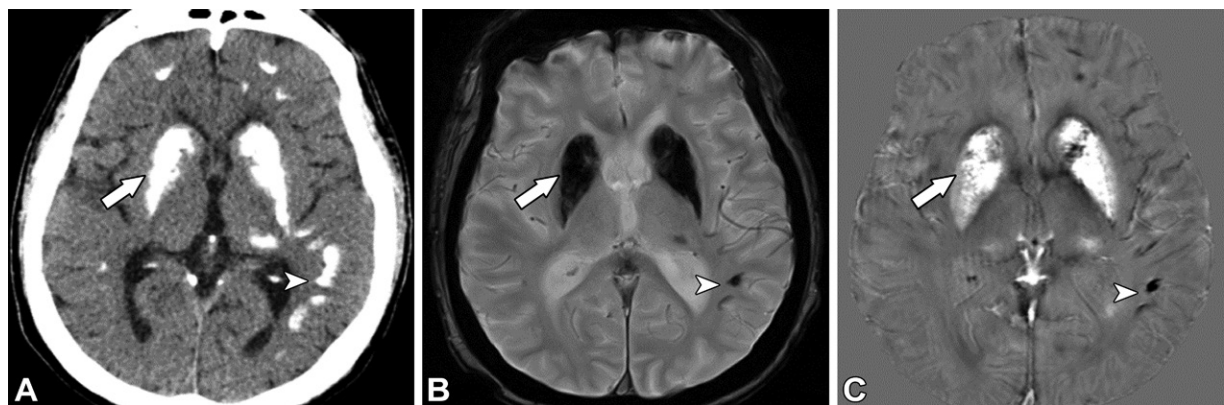

Figure 11.   Fahr disease or idiopathic basal ganglia calcification in a 32-year-old man. **(A)** Axial CT image shows high attenuation of the basal ganglia (arrow) and subcortical area (arrowhead). **(B)** Axial T2*-weighted MR image shows areas of low signal intensity in the subcortical area (arrowhead) and basal ganglia (arrow). **(C)** QSM image demonstrates low contrast in the subcortical lesion (arrowhead), indicating calcification, but the basal ganglia demonstrate high contrast (arrow), suggesting mineralization with paramagnetic inorganic substances.

Parkinson Disease and Diseases Manifesting with Parkinsonism

Parkinson disease is a progressive movement disorder, and its pathologic basis is loss of dopaminergic neurons and the appearance of Lewy bodies in the striatum pathway. Patients with Parkinson disease have been proved with pathologic analysis to have increased brain iron levels, especially in the substantia nigra, and the excessive iron deposition contributes to oxidative stress and neuronal death (33,34). QSM has been actively applied to help study patients with Parkinson disease, and iron deposition in the substantia nigra has been reported. In a study that compared patients with Parkinson disease and healthy controls by using QSM and R2* values, QSM was more accurate in depicting abnormal iron deposition than R2* (35). QSM can delineate increased iron levels as high contrast in the substantia nigra and

red nucleus in the earliest stages of the disease, indicating that QSM may potentially serve as an early diagnostic tool for Parkinson disease (36). Furthermore, QSM depicts the increase in iron levels over the disease course, which correlates with disease progression (37).

Parkinsonism can be observed in a variety of diseases, including multiple system atrophy, which is subdivided into multiple system atrophy with predominant parkinsonism (MSA-P), multiple system atrophy with predominant cerebellar ataxia (MSA-C), and progressive supranuclear palsy (PSP). Although there are consensus diagnostic criteria for these diseases, the clinical symptoms are often similar in the early stages of the disease, thereby leading to difficulties in diagnosis (38). Increased magnetic susceptibility of the basal ganglia, substantia nigra, and red nuclei has been reported in these diseases that manifest

with parkinsonism. However, in terms of differentiation from these diseases, QSM alone can be used to help differentiate between MSA-P and PSP, since iron deposits in the posterior lateral part of the putamen are prominent with MSA-P, whereas the iron deposits are prominent in the globus pallidus in PSP (Fig 12) (39,40).

Amyotrophic Lateral Sclerosis

Amyotrophic lateral sclerosis (ALS) is a progressive neurodegenerative disorder characterized by cortical and spinal motor neuron dysfunction. Some patients with ALS demonstrate hypointense signal in the motor cortex at T2*-weighted imaging. QSM shows increased magnetic susceptibility as high contrast in the motor cortex, which has great potential to be a sensitive diagnostic and prognostic marker in ALS (Fig 13). Meanwhile, the high contrast at QSM in the motor cortex is also depicted in normal aging and chronic multiple infarctions, which is supposed to be caused by neurodegeneration with iron deposition. However, iron deposition in ALS has been reported to be more severe than that of aging and infarctions (41).

Alzheimer Disease

Alzheimer disease is a progressive neurodegenerative disease characterized by senile plaques and neurofibrillary tangles, resulting in loss of neuronal connections in the brain. Amyloid plaque overloads lead to iron aggregates in the brain tissue, causing chemical reduction of redox-inactive ferric irons to redox-active ferrous iron. The increase in iron is closely related to increased production of amyloid-β peptides, resulting in oxidative stress and resultant neuronal damage (42). Studies on Alzheimer disease using QSM have discussed the increase of brain iron content and suggested that increased brain iron together with β-amyloid in the hippocampus, amygdala, precuneus, and thalamus is associated with lower cognitive functioning in individuals with mild cognitive impairment or Alzheimer disease (43,44).

Recent reports have shown that iron deposition in the hippocampus that is depicted with QSM in older adults with normal cognitive function negatively correlates with global cognitive scores, which coincides with amyloid accumulation visible at PET. Therefore, QSM can serve as a novel imaging biomarker for evaluating preclinical Alzheimer disease or iron deposition associated with β-amyloid

Multiple Sclerosis

Multiple sclerosis is a demyelinating disease in which the myelin sheaths in the brain and spinal cord are damaged. QSM has been actively used
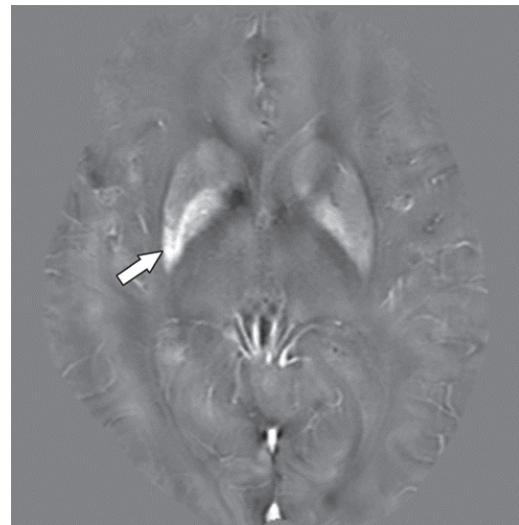

Figure 12. Multiple system atrophy in a 67-year-old man with parkinsonism with left-sided predominance. QSM image shows high contrast in the lateral dorsal lesion in the right putamen (arrow), which is suggestive of a typical degenerative site in MSA-P.

in studying multiple sclerosis and can demonstrate retention of iron among a subset of chronic lesions. Enhancing multiple sclerosis lesions depicted at gadolinium-based contrast agent (GBCA)–enhanced T1-weighted MR imaging are representative of the breakdown of the blood-brain barrier and acute disease activity. In this acute phase, no increase in magnetic susceptibility is observed (Fig 14) (45).

As the blood-brain barrier closes, lesions transition to the chronic stage. Chronic active multiple sclerosis lesions in the initial few (~4) years have been shown to have high-contrast rims at QSM, characterized by iron-enriched activated microglia and macrophages (45,46). Then, they gradually dissipate back to a susceptibility value similar to that of normal-appearing white matter (Fig 15) (45). Therefore, serial QSM provides information regarding the current state of inflammation within multiple sclerosis lesions. Lesions with no increase in magnetic susceptibility are acute or older than 5 years, while those with increased magnetic susceptibility indicate the possibility of several weeks to years after onset. These transitions may be used to prove dissemination in time.

Additionally, neuromyelitis optica spectrum disorder (NMOSD), a demyelinating disease, may demonstrate imaging findings similar to those of the early stages of multiple sclerosis. However, NMOSD does not show paramagnetic rims around lesions that are visible with fluid-attenuated inversion recovery (FLAIR) sequences, and this finding can be used to differentiate NMOSD from multiple sclerosis (47).
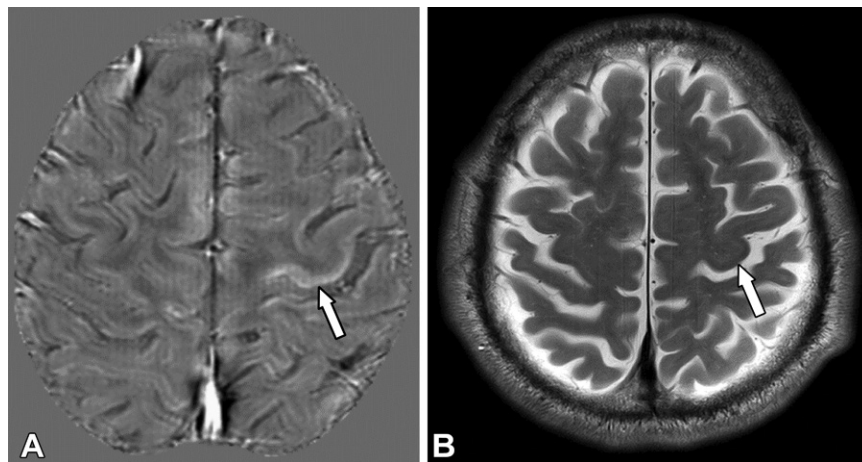
Figure 13. ALS in a 42-year-old woman with slowly progressive muscle atrophy. **(A)** Axial QSM image demonstrates a high-contrast area (arrow) in the cortex of the left precentral gyrus. **(B)** Axial T2-weighted MR image demonstrates how the high-contrast area in **A** is difficult to depict with T2-weighted imaging (arrow).
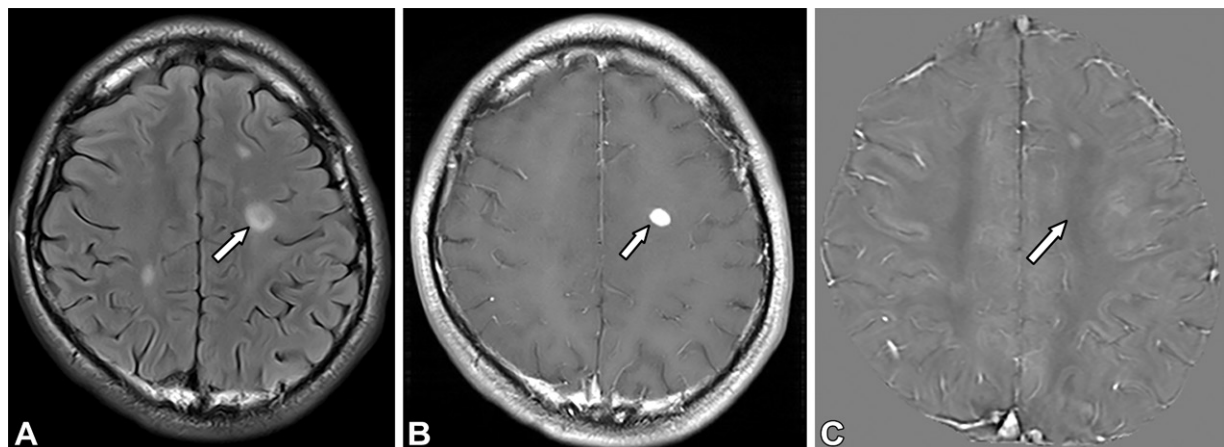

Figure 14.   Multiple sclerosis in a 28-year-old woman with mild numbness in the right side of the body. **(A, B)** Axial fluid-attenuated inversion recovery (FLAIR) **(A)** and GBCA-enhanced T1-weighted **(B)** MR images show hyperintensity (arrow) in the left frontal lobe, indicating acute demyelination. **(C)** Axial QSM image shows no increase in the magnetic susceptibility of the lesion (arrow).
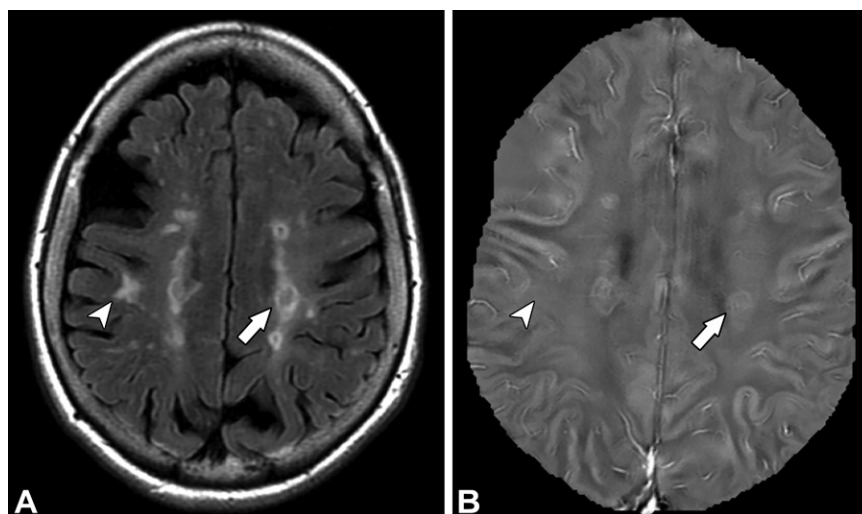

Figure 15.   Multiple sclerosis in a 66-year-old man. **(A)** Axial FLAIR MR image shows multiple hyperintense lesions in the periventricular white matter (arrow) and U-fiber lesions (arrowhead) with no changes on the follow-up images. **(B)** Axial QSM image demonstrates high contrast (arrow) or isocontrast (arrowhead). High-contrast lesions were estimated to be aged from several weeks to years (early-to-intermediate disease). Lesions with isocontrast were estimated to be 5 years old or older (chronic disease).

Gadolinium Deposition

GBCAs have been widely used for contrast-enhanced MRI in central nervous system disorders such as brain tumors and demyelinating diseases. Gadolinium accumulation has recently gained at-

tention. Kanda et al (48) reported first that linear GBCAs are less stable than macrocyclic GBCAs, and therefore have a higher deposition amount, and that gadolinium deposition after serial linear GBCA administrations can be evaluated at
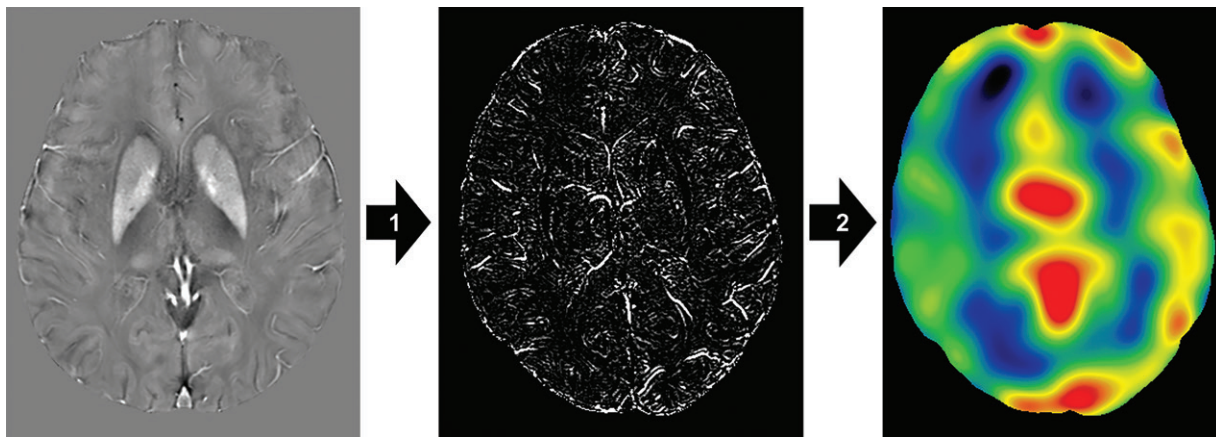
Figure 16. Process steps of converting QSM into OEF mapping. The QSM-OEF process consists of the following steps: vein extraction from the QSM image by using an appropriate threshold *(1)* and estimation of OEF based on the venous susceptibility *(2)*.

T1-weighted imaging in the dentate nucleus and globus pallidus because of T1 shortening.

Although gadolinium associated with macrocyclic GBCA use has been pathologically proved to be deposited in the brain, the amount of gadolinium deposition is low because of the high stability of these conjugates, and abnormal signal intensity cannot be depicted at T1-weighted imaging. In contrast, because gadolinium is a strong paramagnetic substance, susceptibility values should be theoretically elevated when gadolinium deposition is observed. Indeed, deposition in the cerebellar dentate nucleus has been evaluated with QSM (48,49). Region-of-interest analysis with QSM can be used to evaluate increased magnetic susceptibility of the cerebellar dentate nucleus and globus pallidus after serial macrocyclic GBCA administrations (50). Therefore, QSM can depict small amounts of gadolinium deposits after serial GBCA administrations that cannot be depicted at T1-weighted imaging. However, the clinical significance of this gadolinium deposition in the brain remains uncertain.

Oxygen Extraction Fraction

Since deoxyhemoglobin is paramagnetic compared with brain tissue, SWI is frequently used to perform imaging in cerebral venous vascular networks. QSM can help quantitatively estimate the oxygen saturation in venous vessels because of the linear relationship between susceptibility and deoxyhemoglobin content (51,52). Oxygen extraction fraction (OEF), calculated from the cerebral oxygen metabolic rate and cerebral blood flow at oxygen 15–labeled water (^{15}O-water) PET, is an important measurable parameter of cerebral metabolism and can provide information about the relative deficit in cerebral blood supply to tissue oxygen demand (called misery perfusion). Although ^{15}O-water PET is

generally recognized as the reference standard for OEF measurements, ^{15}O-water PET has disadvantages such as limited availability, high invasiveness, and radiation exposure.

The theory behind generating OEF maps from QSM is based on the idea that the susceptibility of veins is higher than that of brain parenchyma because of the elevated deoxyhemoglobin concentration. The OEF is calculated by using the magnetic susceptibility of the cortical veins in the region of interest placed on the venous extraction images from QSM. This method is summarized in Figures 16 and E3 as previously reported (53).

In a study of patients with chronic ischemia, a high correlation between QSM-OEF and PET-OEF was found in those with elevated OEF (52). Since the magnetic susceptibility effect is proportional to the static magnetic field strength, 7-T MRI provides more detailed images, and a higher correlation between QSM-OEF and PET-OEF has been reported in cases of unilateral internal carotid artery stenosis (Fig 17) (54). A recent study demonstrated that preoperative QSM-OEF in 7-T MR images could help identify patients at risk for cerebral hyperperfusion after carotid endarterectomy in patients with unilateral internal carotid artery stenosis (55). Interestingly, neuropsychiatric SLE often shows no abnormalities at conventional MRI, suggesting some metabolic or functional changes. The QSM-OEF has been reported to be elevated in cases of neuropsychiatric SLE and is associated with SLE activity, suggesting that the elevated OEF is an indication of reactive changes of the small vessels that may occur as a result of the neuroinflammatory activity of SLE (56).

QSM Outside the Brain

As mentioned earlier, most clinical applications of QSM to date have been in the brain. Characterization of magnetic susceptibility outside the
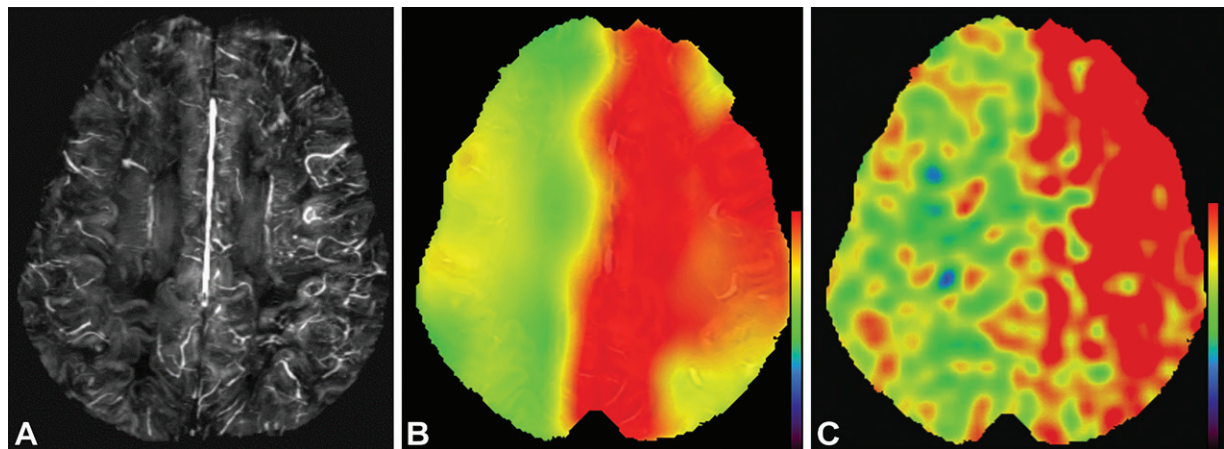
Figure 17. Left middle cerebral artery occlusion in a 74-year-old man. **(A)** Axial partial MIP image from QSM at 7-T MRI shows enhanced cortical veins in the left cerebral hemisphere compared with those on the contralateral side, suggesting increased deoxy-hemoglobin levels. **(B)** Axial QSM-OEF map shows elevated OEF values in the left cerebral hemisphere. **(C)** Axial ^{15}O-water PET image also shows elevated OEF values in the left cerebral hemisphere.
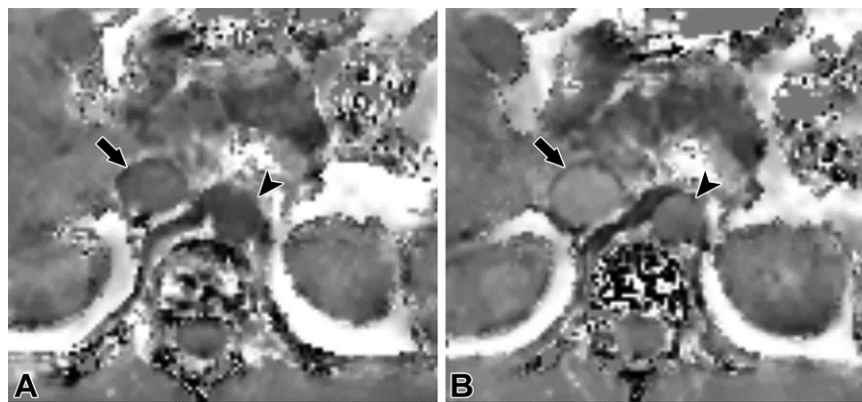

Figure 18. Axial QSM images in the abdomen obtained at the beginning of a breath hold **(A)** and after a 3-minute breath hold **(B)** show increased high contrast in the aorta (arrowhead) and inferior vena cava (arrow), reflecting the increase in deoxyhemoglobin level associated with breath holding.

brain is currently an active area of research. However, adaptation of QSM reconstructions from the brain to other body parts has multiple problems that must be overcome, including the effects of movements such as respirations, heartbeats, and peristalsis, as well as the presence of fat. Fat has a different resonance frequency at MRI and significantly higher magnetic susceptibility than other body tissues; it therefore produces artifacts because of the difference in magnetic susceptibility in regions adjacent to fat.

The source images are acquired by using an accelerated sequence with breath holding that effectively stops respiratory motion during the data acquisition. Several methods for QSM reconstruction of the abdomen have been reported. For example, Sharma et al (57) applied a chemical shift–encoded reconstruction to help estimate the field map and incorporated prior information of the fat distribution into the susceptibility mapping algorithm to determine bulk susceptibility in the liver. Sato et al (58) applied the water-fat separation method: susceptibilities in these two regions were calculated separately and then

combined, and susceptibility in the water region was calculated by using the fat region as a background susceptibility source to remove shading artifacts. On the abdominal QSM images generated with this method, the temporal changes in deoxyhemoglobin with breath holding can be visualized, as shown in Figure 18.

Regarding QSM use in areas other than the brain, the liver is a commonly studied organ. Although R2* has demonstrated good correlation with liver iron content, fibrosis, fat, and edema, other cellular pathologic conditions may interfere with R2* estimation of liver iron content (57). QSM eliminates such cellular interferences for mapping iron deposition. It demonstrates the mixture of fibrosis and iron deposition as well as the advancement of fibrosis more precisely than R2* (59,60). Figure 19 demonstrates that the magnetic susceptibility of the liver in patients with cirrhosis is clearly higher than that in healthy patients.

Azuma et al (61) and Ikebe et al (62) characterized the composition of carotid plaques and quantified the degree of intraplaque hemorrhage and iron deposits compared with pathologic findings in
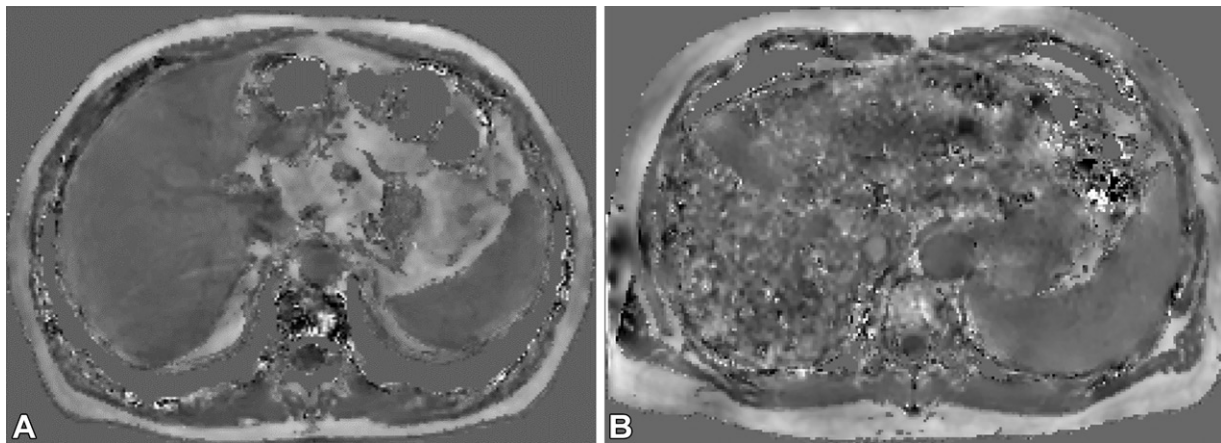
Figure 19.   Liver cirrhosis. **(A)** Axial QSM image in a healthy volunteer shows that the magnetic susceptibility values of the liver and spleen are almost the same. **(B)** Axial QSM image in a 63-year-old man with liver cirrhosis depicts how the magnetic susceptibility of the liver parenchyma is heterogeneously elevated, suggesting iron deposition associated with liver cirrhosis.

vivo and ex vivo (Fig 20). Intraplaque hemorrhage in the carotid artery is related to an increased risk of plaque rupture and plays a critical role in stratifying the risk of future events in patients with carotid atherosclerosis. The imaging modalities for evaluation of plaque composition are US and multiparametric qualitative conventional MRI (ie, T1- and T2*-weighted MRI). QSM can be a novel imaging approach for characterizing the composition of carotid plaques, including intraplaque hemorrhage, iron deposition, lipid, necrotic core, and calcification (61,62).

Other reports have used QSM to help assess early articular cartilage damage in osteoarthritis and found decreased magnetic susceptibility of articular cartilage in the patient group because of microstructure alterations or changes in the constituents of the cartilage (63). Bone studies demonstrated that the results of quantitative CT correlated with the magnetic susceptibility obtained with QSM in postmenopausal women (an assessment of osteoporosis) (64). Further studies have assessed noninvasive measurement of mixed venous oxygen saturation in the lumen of the heart by using QSM, which is a noninvasive measurement of placental oxygenation (65); a feasibility study on the difference in the magnetic susceptibility of the cortex and medulla of the kidney by using QSM (66); and a study on depiction of intraprostatic calcification at CT by using QSM (67). The potential applications of QSM in iron quantification and metabolism currently performed by using R2* value may provide new insights into disease development and diagnosis.

Conclusion
QSM provides a quantitative contrast based on magnetic susceptibility and can be used for characterization of tissue magnetic susceptibility.
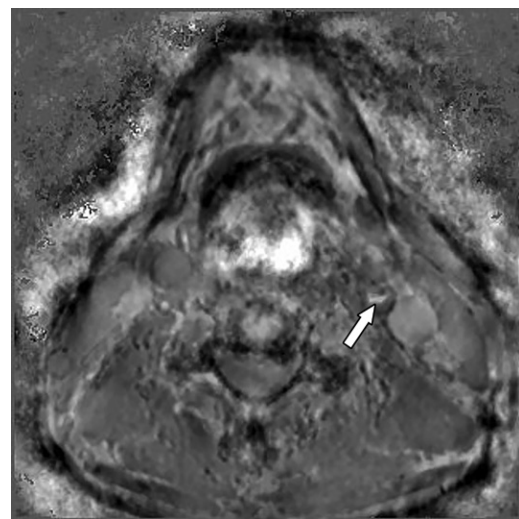

Figure 20.   Left internal carotid artery stenosis in a 68-year-old man. QSM image depicts a plaque with high contrast (arrow) that was found dorsally within the left internal carotid artery. Pathologic analysis revealed hemorrhagic plaque.

QSM has the potential to provide unique causal and diagnostic information on changes in tissue compositions such as those seen in myelin, as well as the presence of calcification or hemorrhage, distribution of iron deposition, and deoxyhemoglobin levels. Despite the complicated image reconstruction, QSM has the potential to replace SWI. Quantitative analysis by using QSM is useful for elucidating the underlying mechanisms of neurodegenerative diseases with excessive iron deposition and can also provide functional information such as the OEF. The direct mapping of tissue properties may offer new insights into disease development and diagnosis, and the application field of QSM will most likely expand from the brain to other organs.

References

1. Haacke EM, Liu S, Buch S, Zheng W, Wu D, Ye Y. Quantitative susceptibility mapping: current status and future directions. Magn Reson Imaging 2015;33(1):1–25.

2. Wang Y, Spincemaille P, Liu Z, et al. Clinical quantitative susceptibility mapping (QSM): biometal imaging and its emerging roles in patient care. J Magn Reson Imaging 2017;46(4):951–971.

3. Rudko DA, Klassen LM, de Chickera SN, Gati JS, Dekaban GA, Menon RS. Origins of R2* orientation dependence in gray and white matter. Proc Natl Acad Sci U S A 2014;111(1):E159–E167.

4. Liu T, Wisnieff C, Lou M, Chen W, Spincemaille P, Wang Y. Nonlinear formulation of the magnetic field to source relationship for robust quantitative susceptibility mapping. Magn Reson Med 2013;69(2):467–476.

5. Deistung A, Schweser F, Reichenbach JR. Overview of quantitative susceptibility mapping. NMR Biomed 2017;30(4):e3569.

6. Wang Y, Liu T. Quantitative susceptibility mapping (QSM): decoding MRI data for a tissue magnetic biomarker. Magn Reson Med 2015;73(1):82–101.

7. Wu B, Li W, Avram AV, Gho SM, Liu C. Fast and tissue-optimized mapping of magnetic susceptibility and T2* with multi-echo and multi-shot spirals. Neuroimage 2012;59(1):297–305.

8. Liu T, Spincemaille P, de Rochefort L, Kressler B, Wang Y. Calculation of susceptibility through multiple orientation sampling (COSMOS): a method for conditioning the inverse problem from measured magnetic field map to susceptibility source image in MRI. Magn Reson Med 2009;61(1):196–204.

9. Haller S, Haacke EM, Thurnher MM, Barkhof F. Susceptibility-weighted Imaging: Technical Essentials and Clinical Neurologic Applications. Radiology 2021;299(1):3–26.

10. Reichenbach JR, Schweser F, Serres B, Deistung A. Quantitative Susceptibility Mapping: Concepts and Applications. Clin Neuroradiol 2015;25(suppl 2):225–230.

11. Chen W, Zhu W, Kovanlikaya I, et al. Intracranial calcifications and hemorrhages: characterization with quantitative susceptibility mapping. Radiology 2014;270(2):496–505.

12. Sun H, Klahr AC, Kate M, et al. Quantitative Susceptibility Mapping for Following Intracranial Hemorrhage. Radiology 2018;288(3):830–839.

13. De A, Sun H, Emery DJ, Butcher KS, Wilman AH. Rapid quantitative susceptibility mapping of intracerebral hemorrhage. J Magn Reson Imaging 2020;51(3):712–718.

14. Löbel U, Sedlacik J, Sabin ND, et al. Three-dimensional susceptibility-weighted imaging and two-dimensional T2*-weighted gradient-echo imaging of intratumoral hemorrhages in pediatric diffuse intrinsic pontine glioma. Neuroradiology 2010;52(12):1167–1177.

15. Bähr O, Hattingen E, Rieger J, Steinbach JP. Bevacizumab-induced tumor calcifications as a surrogate marker of outcome in patients with glioblastoma. Neuro Oncol 2011;13(9):1020–1029.

16. Lei P, Ayton S, Finkelstein DI, et al. Tau deficiency induces parkinsonism with dementia by impairing APP-mediated iron export. Nat Med 2012;18(2):291–295.

17. Haacke EM, Cheng NY, House MJ, et al. Imaging iron stores in the brain using magnetic resonance imaging. Magn Reson Imaging 2005;23(1):1–25.

18. Aquino D, Bizzi A, Grisoli M, et al. Age-related iron deposition in the basal ganglia: quantitative analysis in healthy subjects. Radiology 2009;252(1):165–172.

19. Li W, Wu B, Batrachenko A, et al. Differential developmental trajectories of magnetic susceptibility in human brain gray and white matter over the lifespan. Hum Brain Mapp 2014;35(6):2698–2713.

20. Alkemade A, de Hollander G, Keuken MC, et al. Comparison of T2*-weighted and QSM contrasts in Parkinson's disease to visualize the STN with MRI. PLoS One 2017;12(4):e0176130.

21. Fukunaga M, Li TQ, van Gelderen P, et al. Layer-specific variation of iron content in cerebral cortex as a source of MRI contrast. Proc Natl Acad Sci U S A 2010;107(8):3834–3839.

22. Langkammer C, Krebs N, Goessler W, et al. Susceptibility induced gray-white matter MRI contrast in the human brain. Neuroimage 2012;59(2):1413–1419.

23. Wiethoff S, Houlden H. Neurodegeneration with brain iron accumulation. Handb Clin Neurol 2017;145:157–166.

24. Kimura Y, Sato N, Ishiyama A, et al. Serial MRI alterations of pediatric patients with beta-propeller protein associated neurodegeneration (BPAN). J Neuroradiol 2021;48(2):88–93.

25. Donzuso G, Mostile G, Nicoletti A, Zappia M. Basal ganglia calcifications (Fahr's syndrome): related conditions and clinical features. Neurol Sci 2019;40(11):2251–2263. [Published correction appears in Neurol Sci 2019;40(11):2265.]

26. Peters MEM, de Brouwer EJM, Bartstra JW, et al. Mechanisms of calcification in Fahr disease and exposure of potential therapeutic targets. Neurol Clin Pract 2020;10(5):449–457.

27. Valdés Hernández MC, Maconick LC, Tan EM, Wardlaw JM. Identification of mineral deposits in the brain on radiological images: a systematic review. Eur Radiol 2012;22(11):2371–2381.

28. Lee S, Nam Y, Jang J, et al. Deep gray matter iron measurement in patients with liver cirrhosis using quantitative susceptibility mapping: relationship with pallidal T1 hyperintensity. J Magn Reson Imaging 2018;47(5):1342–1349.

29. Ogasawara A, Kakeda S, Watanabe K, et al. Quantitative susceptibility mapping in patients with systemic lupus erythematosus: detection of abnormalities in normal-appearing basal ganglia. Eur Radiol 2016;26(4):1056–1063.

30. Doganay S, Gumus K, Koc G, et al. Magnetic Susceptibility Changes in the Basal Ganglia and Brain Stem of Patients with Wilson's Disease: Evaluation with Quantitative Susceptibility Mapping. Magn Reson Med Sci 2018;17(1):73–79.

31. Yao S, Zhong Y, Xu Y, et al. Quantitative Susceptibility Mapping Reveals an Association between Brain Iron Load and Depression Severity. Front Hum Neurosci 2017;11:442.

32. Tang S, Xu Y, Liu X, et al. Quantitative susceptibility mapping shows lower brain iron content in children with autism. Eur Radiol 2021;31(4):2073–2083.

33. Ward RJ, Zucca FA, Duyn JH, Crichton RR, Zecca L. The role of iron in brain ageing and neurodegenerative disorders. Lancet Neurol 2014;13(10):1045–1060.

34. Kordower JH, Olanow CW, Dodiya HB, et al. Disease duration and the integrity of the nigrostriatal system in Parkinson's disease. Brain 2013;136(Pt 8):2419–2431.

35. Murakami Y, Kakeda S, Watanabe K, et al. Usefulness of quantitative susceptibility mapping for the diagnosis of Parkinson disease. AJNR Am J Neuroradiol 2015;36(6):1102–1108.

36. Kim EY, Sung YH, Shin HG, Noh Y, Nam Y, Lee J. Diagnosis of Early-Stage Idiopathic Parkinson's Disease Using High-Resolution Quantitative Susceptibility Mapping Combined with Histogram Analysis in the Substantia Nigra at 3 T. J Clin Neurol 2018;14(1):90–97.

37. Guan X, Xuan M, Gu Q, et al. Regionally progressive accumulation of iron in Parkinson's disease as measured by quantitative susceptibility mapping. NMR Biomed 2017;30(4):e3489.

38. Hughes AJ, Daniel SE, Ben-Shlomo Y, Lees AJ. The accuracy of diagnosis of parkinsonian syndromes in a specialist movement disorder service. Brain 2002;125(Pt 4):861–870.

39. Ito K, Ohtsuka C, Yoshioka K, et al. Differential diagnosis of parkinsonism by a combined use of diffusion kurtosis imaging and quantitative susceptibility mapping. Neuroradiology 2017;59(8):759–769.

40. Sjöström H, Granberg T, Westman E, Svenningsson P. Quantitative susceptibility mapping differentiates between parkinsonian disorders. Parkinsonism Relat Disord 2017;44:51–57.

41. Lee JY, Lee YJ, Park DW, et al. Quantitative susceptibility mapping of the motor cortex: a comparison of susceptibility among patients with amyotrophic lateral sclerosis, cerebrovascular disease, and healthy controls. Neuroradiology 2017;59(12):1213–1222.

42. Everett J, Céspedes E, Shelford LR, et al. Ferrous iron formation following the co-aggregation of ferric iron and the Alzheimer's disease peptide β-amyloid (1-42). J R Soc Interface 2014;11(95):20140165.

43. Ayton S, Fazlollahi A, Bourgeat P, et al. Cerebral quantitative susceptibility mapping predicts amyloid-β-related cognitive decline. Brain 2017;140(8):2112–2119.

44. Kim HG, Park S, Rhee HY, et al. Quantitative susceptibility mapping to evaluate the early stage of Alzheimer's disease. Neuroimage Clin 2017;16:429–438.

45. Zhang S, Nguyen TD, Hurtado Rúa SM, et al. Quantitative Susceptibility Mapping of Time-Dependent Susceptibility Changes in Multiple Sclerosis Lesions. AJNR Am J Neuroradiol 2019;40(6):987–993.

46. Wisnieff C, Ramanan S, Olesik J, Gauthier S, Wang Y, Pitt D. Quantitative susceptibility mapping (QSM) of white matter multiple sclerosis lesions: interpreting positive susceptibility and the presence of iron. Magn Reson Med 2015;74(2):564–570.

47. Jang J, Nam Y, Choi Y, et al. Paramagnetic Rims in Multiple Sclerosis and Neuromyelitis Optica Spectrum Disorder: A Quantitative Susceptibility Mapping Study with 3-T MRI. J Clin Neurol 2020;16(4):562–572.

48. Kanda T, Osawa M, Oba H, et al. High Signal Intensity in Dentate Nucleus on Unenhanced T1-weighted MR Images: Association with Linear versus Macrocyclic Gadolinium Chelate Administration. Radiology 2015;275(3):803–809.

49. Hinoda T, Fushimi Y, Okada T, et al. Quantitative assessment of gadolinium deposition in dentate nucleus using quantitative susceptibility mapping. J Magn Reson Imaging 2017;45(5):1352–1358.

50. Choi Y, Jang J, Kim J, et al. MRI and Quantitative Magnetic Susceptibility Maps of the Brain after Serial Administration of Gadobutrol: A Longitudinal Follow-up Study. Radiology 2020;297(1):143–150.

51. Ruetten PPR, Gillard JH, Graves MJ. Introduction to Quantitative Susceptibility Mapping and Susceptibility Weighted Imaging. Br J Radiol 2019;92(1101):20181016.

52. Zhang J, Zhou D, Nguyen TD, Spincemaille P, Gupta A, Wang Y. Cerebral metabolic rate of oxygen ($CMRO_2$) mapping with hyperventilation challenge using quantitative susceptibility mapping (QSM). Magn Reson Med 2017;77(5):1762–1773.

53. Kudo K, Liu T, Murakami T, et al. Oxygen extraction fraction measurement using quantitative susceptibility mapping: comparison with positron emission tomography. J Cereb Blood Flow Metab 2016;36(8):1424–1433.

54. Uwano I, Kudo K, Sato R, et al. Noninvasive Assessment of Oxygen Extraction Fraction in Chronic Ischemia Using Quantitative Susceptibility Mapping at 7 Tesla. Stroke 2017;48(8):2136–2141.

55. Nomura JI, Uwano I, Sasaki M, et al. Preoperative Cerebral Oxygen Extraction Fraction Imaging Generated from 7T MR Quantitative Susceptibility Mapping Predicts Development of Cerebral Hyperperfusion following Carotid Endarterectomy. AJNR Am J Neuroradiol 2017;38(12):2327–2333.

56. Miyata M, Kakeda S, Kudo K, et al. Evaluation of oxygen extraction fraction in systemic lupus erythematosus patients using quantitative susceptibility mapping. J Cereb Blood Flow Metab 2019;39(8):1648–1658.

57. Sharma SD, Hernando D, Horng DE, Reeder SB. Quantitative susceptibility mapping in the abdomen as an imaging biomarker of hepatic iron overload. Magn Reson Med 2015;74(3):673–683.

58. Sato R, Shirai T, Soutome Y, Bito Y, Ochi H. Quantitative susceptibility mapping of prostate with separate calculations for water and fat regions for reducing shading artifacts. Magn Reson Imaging 2020;66:22–29.

59. Li J, Lin H, Liu T, et al. Quantitative susceptibility mapping (QSM) minimizes interference from cellular pathology in R2* estimation of liver iron concentration. J Magn Reson Imaging 2018;48(4):1069–1079.

60. Yoshikawa M, Kudo K, Harada T, et al. Quantitative Susceptibility Mapping versus R2*-based Histogram Analysis for Evaluating Liver Fibrosis: Preliminary Results. Magn Reson Med Sci 2021. 10.2463/mrms.mp.2020-0175. Published online September 4, 2021.

61. Azuma M, Maekawa K, Yamashita A, et al. Characterization of Carotid Plaque Components by Quantitative Susceptibility Mapping. AJNR Am J Neuroradiol 2020;41(2):310–317.

62. Ikebe Y, Ishimaru H, Imai H, et al. Quantitative Susceptibility Mapping for Carotid Atherosclerotic Plaques: A Pilot Study. Magn Reson Med Sci 2020;19(2):135–140.

63. Wei H, Lin H, Qin L, et al. Quantitative susceptibility mapping of articular cartilage in patients with osteoarthritis at 3T. J Magn Reson Imaging 2019;49(6):1665–1675.

64. Chen Y, Guo Y, Zhang X, Mei Y, Feng Y, Zhang X. Bone susceptibility mapping with MRI is an alternative and reliable biomarker of osteoporosis in postmenopausal women. Eur Radiol 2018;28(12):5027–5034.

65. Zun Z, Kapse K, Quistorff J, et al. Feasibility of QSM in the human placenta. Magn Reson Med 2021;85(3):1272–1281.

66. Bechler E, Stabinska J, Thiel T, et al. Feasibility of quantitative susceptibility mapping (QSM) of the human kidney. MAGMA 2021;34(3):389–397.

67. Straub S, Laun FB, Emmerich J, et al. Potential of quantitative susceptibility mapping for detection of prostatic calcifications. J Magn Reson Imaging 2017;45(3):889–898.